

Spinel ferrite nanocrystals embedded inside ZnO: magnetic, electronic and magneto-transport properties

Shengqiang Zhou,^{1,*} K. Potzger,¹ Qingyu Xu,² K. Kuepper,¹ G. Talut,¹ D. Markó,¹
A. Mücklich,¹ M. Helm,¹ J. Fassbender,¹ E. Arenholz,³ and H. Schmidt¹

¹*Institute of Ion Beam Physics and Materials Research, Forschungszentrum
Dresden-Rossendorf, P.O. Box 510119, 01314 Dresden, Germany*

²*Department of Physics, Southeast University, Nanjing 211189, China*

³*Advanced Light Source, Lawrence Berkeley National Laboratory, Berkeley, California 94720, USA*

(Dated: January 23, 2018)

In this paper we show that spinel ferrite nanocrystals (NiFe_2O_4 , and CoFe_2O_4) can be texturally embedded inside a ZnO matrix by ion implantation and post-annealing. The two kinds of ferrites show different magnetic properties, *e.g.* coercivity and magnetization. Anomalous Hall effect and positive magnetoresistance have been observed. Our study suggests a ferrimagnet/semiconductor hybrid system for potential applications in magneto-electronics. This hybrid system can be tuned by selecting different transition metal ions (from Mn to Zn) to obtain various magnetic and electronic properties.

I. INTRODUCTION

Spinel ferrites are materials with rich magnetic and electronic properties¹. As bulk materials, they can be half-metallic (such as Fe_3O_4) or insulating (most spinel ferrites), ferrimagnetic (most spinel ferrites) or anti-ferromagnetic (ZnFe_2O_4). Insulating ferrites (such as NiFe_2O_4 and $\text{ZnNiFe}_2\text{O}_4$) are usually referred to as magnetic insulators. These kinds of materials are technologically important with various applications as permanent magnets, microwave devices, and magnetic recording media. Physically the magnetic and electronic properties of spinel ferrites are determined by the cation distribution among the tetrahedral (A) and octahedral (B) sites. The growth of low-dimensional spinel ferrites of both thin films and nanoparticles has shown the possibility to tune the cation distribution, therefore resulting in magnetic and electrical properties drastically different from bulk materials. Lüders *et al.* have shown that the conductivity of NiFe_2O_4 thin films can be tuned over five orders of magnitude by varying the growth atmosphere². The sites of Fe^{3+} can be changed from A to B sites in ZnFe_2O_4 nanoparticles, resulting in ferrimagnetism³. Geiler *et al.* proposed a method to design and control the cation distribution in hexagonal $\text{BaFe}_{12-x}\text{Mn}_x\text{O}_{19}$ ferrites at an atomic scale, which results in the increase of magnetic moment and Néel temperature⁴. Moreover, most of transition metals (TM) can form solid solutions with Fe_3O_4 , resulting in $\text{TM}_x\text{Fe}_{3-x}\text{O}_4$ spinel alloys with x ranging from 0 to 1, which provides an additional degree of freedom to tune their magnetic and electronic properties^{5,6}. In previous research, anomalous Hall effect and magnetoresistance have been found in spinel ferrite thin films or granules at room temperature, demonstrating spin-polarization of free carriers. Moreover, ferrite thin films NiFe_2O_4 and CoFe_2O_4 with different conductivities have been demonstrated to be useful as electrodes or spin-filter in magnetic tunnel junctions^{2,7,8,9,10}. However, to our knowledge, very limited effort has been spent to

tegrate ferrite oxides with semiconductors. The growth of ferrite oxides requires high temperatures and oxygen environment, which is detrimental to conventional semiconductors like Si and GaAs¹¹. This explains why oxide insulators such as MgO , Al_2O_3 , and SrTiO_3 are mostly used as the substrates to grow ferrite oxides¹². In this paper, we show that TMFe_2O_4 nanocrystals (TM=Ni, Co) can be embedded inside ZnO, and we present a systematic study on their magnetic, electronic, and transport properties. The various ferrites with different magnetic properties synthesized inside a semiconducting matrix open a new avenue for fabricating hybrid systems.

II. EXPERIMENTS

We utilize different methods to characterize the ferrite/ZnO hybrid systems. The aim is to show the similarity in structure, but variability in magnetic, electronic and magneto-transport properties.

Commercial ZnO(0001) single crystals with the thickness of 0.5 mm from Crystec were co-implanted with ⁵⁷Fe and Ni or Co ions at 623 K with a fluence of 4×10^{16} and 2×10^{16} cm^{-2} , respectively. The implantation energy was 80 keV for all three kinds of elements. This energy resulted in the projected range of $R_P = 38, 37, 37$ nm, and the longitudinal straggling of $\Delta R_P = 17, 17, 17$ nm, respectively, for Fe, Co, and Ni. Therefore, the implanted Fe ions are in the same range as the Co and Ni ions. The maximum atomic concentration is about 10% and 5% for Fe and Ni(Co), respectively (TRIM code¹³). The maximum implanted depth is around 80 nm (around 5% of the maximum concentration) from the surface. Annealing was performed in a high vacuum (base pressure $\leq 10^{-6}$ mbar) furnace at 1073 K for 60 minutes. In our previous study we have performed detailed annealing investigation for transition metal implanted ZnO single crystals^{3,14,15}. Briefly, more metallic clusters formed when annealing at mild temperatures (823 K or 923 K),

while the oxidation starts at around 1073 K. Keeping this high temperature, a longer annealing time results in the formation of ferrites in Fe implanted ZnO.

Magnetic properties were measured with superconducting quantum interference device (SQUID, Quantum Design MPMS) magnetometry. The samples were measured with the field along the sample surface. The temperature dependent magnetization measurement was carried out in the following way. The sample was cooled in zero field from above room temperature to 5 K. Then a 50 Oe field was applied, and the zero-field cooled (ZFC) magnetization curve was measured with increasing temperature from 5 to 350 K, after which the field-cooled (FC) magnetization curve was measured in the same field from 350 to 5 K with decreasing temperature.

Structural analysis was performed by synchrotron radiation x-ray diffraction (SR-XRD) and transmission electron microscopy (TEM, FEI Titan). SR-XRD was performed at the Rossendorf beamline (BM20) at the ESRF with an x-ray wavelength of 0.154 nm. The cross-section specimen for TEM investigation was prepared by the conventional method including cutting, glueing, mechanical polishing, and dimpling procedures followed by Ar^+ ion-beam milling until perforation. The ion-milling was performed using a "Gatan PIPS". The milling parameters were: 4 keV, 10 μA ion current at milling angle of 4° with respect to the specimen surface. The area around the hole is electron-transparent (thickness < 100 nm).

Element-specific electronic properties were investigated by X-ray absorption spectroscopy (XAS) and X-ray magnetic circular dichroism (XMCD) at the Fe, Co and Ni $L_{2,3}$ absorption edges. These experiments were performed at beamlines 8.0.1 (XAS) and 6.3.1 (XMCD) of the Advanced Light Source (ALS) in Berkeley, respectively. Both total electron yield (TEY) and total fluorescence yield (TFY) were recorded during the measurement. While TFY is bulk sensitive, TEY probes the near-surface region. For XMCD, the measurement was done at the minimum achievable measurement temperature of 23 K in TEY mode. A magnetic field of ± 2000 Oe was applied parallel to the beam. The grazing angle of the incident light was fixed at 30° with respect to the sample surface.

Conversion electron Mössbauer spectroscopy (CEMS) in constant-acceleration mode at room temperature (RT) was used to investigate the Fe lattice sites, electronic configuration and corresponding magnetic hyperfine fields. The spectra were evaluated with Lorentzian lines using a least squares fit¹⁶. All isomer shifts are given with respect to $\alpha\text{-Fe}$ at RT.

Magnetotransport properties were measured using Van der Pauw geometry with a magnetic field applied perpendicular to the film plane. Fields up to 60 kOe were applied over a wide temperature range from 5 K to 290 K and the carrier concentration and the majority carrier mobility were extracted.

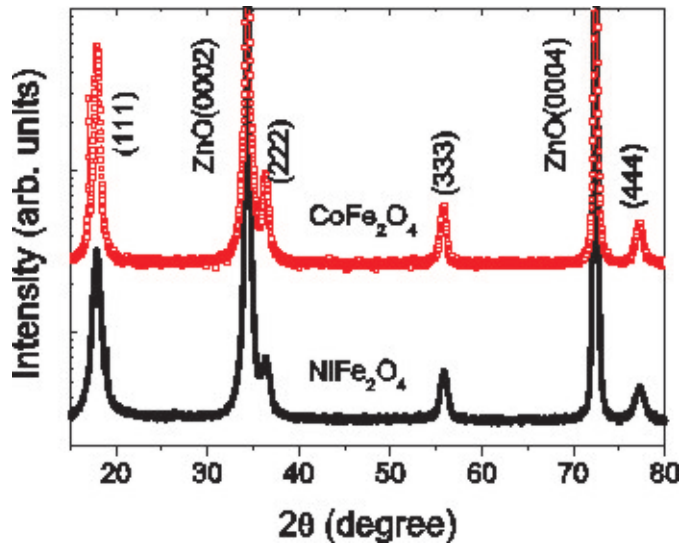


FIG. 1: SR-XRD 2θ - θ scan revealing the formation of NiFe_2O_4 and CoFe_2O_4 in (Ni, Fe) or (Co, Fe) co-implanted ZnO. In both pattern, the diffraction peaks of (111), (222), (333) and (444) from ferrites are clearly visible. The diffraction peaks (0002) and (0004) from ZnO are also indicated. The small and sharp peaks at the left side of CoFe_2O_4 (111) and the right side of NiFe_2O_4 (111) cannot be identified at this stage. The peak at the left side of CoFe_2O_4 (111) could be the forbidden peak of ZnO(0001), which appears due to the lattice damage. However, another forbidden peak of ZnO(0003) does not show up. Note that the two peaks in the two spectra are not at the same angular position, and both correspond to very large lattice distances. Some noise-like peaks are also shown in other paper¹⁷ and could not be identified.

III. RESULTS AND DISCUSSION

A. Structural properties

1. X-ray diffraction

Figure 1 shows the SR-XRD patterns for the annealed samples. Besides the strong peaks from ZnO(0002) and (0004), four small peaks arise for each sample. They are assigned to (111), (222), (333) and (444) diffractions for NiFe_2O_4 and CoFe_2O_4 , respectively. This implies that these nanocrystals are (111) textured inside the ZnO matrix. However, some nanocrystals with (400) orientation have been also observed by TEM as shown below. The crystallite size is estimated using the Scherrer formula¹⁸.

$$d = 0.9\lambda / (\beta \cdot \cos \theta), \quad (1)$$

where λ is the wavelength of the X-ray, θ the Bragg angle, and β the FWHM of 2θ in radians. The average crystallite size is deduced to be around 12 nm and 15 nm for NiFe_2O_4 and CoFe_2O_4 nanocrystals, respectively.

2. TEM

In order to confirm the formation of ferrite nanocrystals, high resolution cross-section TEM was performed

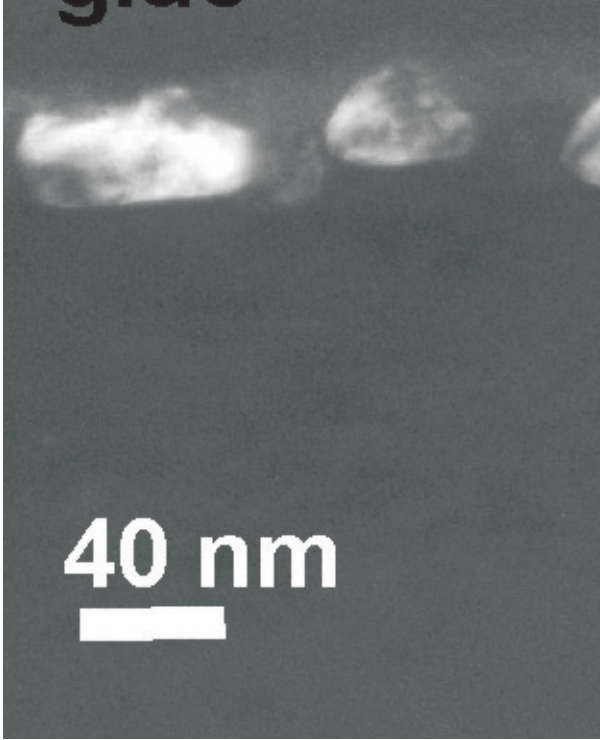


FIG. 2: Cross-section TEM image of Fe and Ni co-implanted ZnO after annealing (a) bright field and (b) dark field.

on selected samples. Fig. 2(a) displays the bright-field TEM images. In an overview, there are three features. The grains of secondary phases are located in the surface region, which are identified as NiFe_2O_4 . Some planar extended defects are indicated by arrows, and are parallel to the basal plane of the ZnO wurtzite structure in a depth of around 60 nm. These extended defects are caused by ion implantation in ZnO¹⁹ and are usually populated at the end of the ion range. The third feature is the dark-spot, which is also located in the depth of unimplanted ZnO. The formation of NiFe_2O_4 at the near-surface depth is also confirmed by the dark-field TEM image as shown in Fig. 2(b) of the same area of Fig. 2(a). The out-diffusion of Fe upon annealing at high temperatures has been observed in ZnO²⁰ as well as in TiO_2 ²¹.

Using high resolution TEM we identified the secondary phase to confirm the XRD results. As shown in Fig. 3(a), the sample was tilted in order to have a better view on the nanocrystals. Note that the lattice planes are more clear in the nanocrystals than that in the ZnO substrate. The inset of Fig. 3(a) is the Fast Fourier Transform (FFT) of the image indicated by a square. The FFT clearly shows the cubic-symmetry of the nanocrystal. The two sets of lattice spacings amount to 0.291 nm and 0.207 nm, and correspond to $\text{NiFe}_2\text{O}_4(220)$ and (004), respectively. Concerning the orientation between NiFe_2O_4 and the ZnO matrix, XRD in general provides the integral information over a large area of the sample, while TEM is a rather localized method. By high resolution TEM, we found some grains with [111] orientation as shown in Fig. 3(b). By FFT two sets of lattice planes are identified to $\text{NiFe}_2\text{O}_4\{111\}$. One is parallel with the sample surface, while the other is around 71° away from the surface [ZnO(0001)]. This is in agreement with a fcc structure of

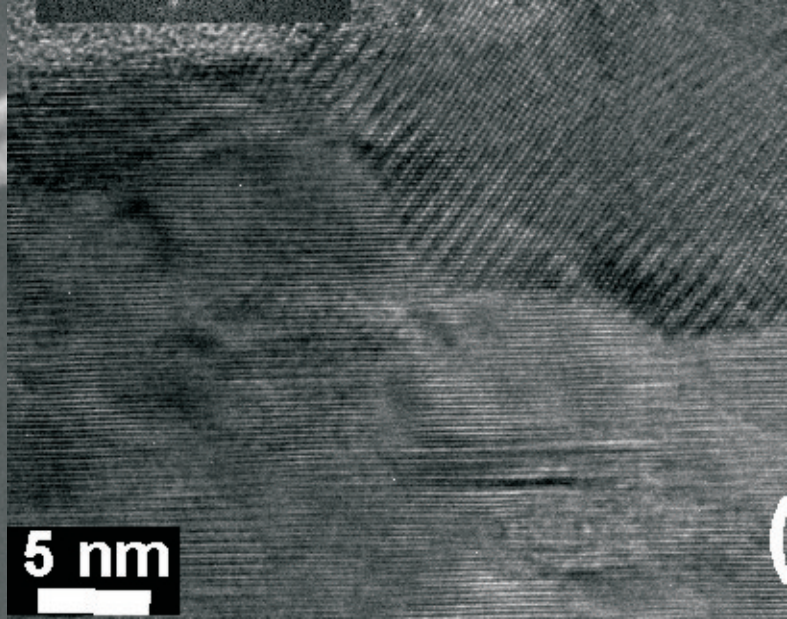


FIG. 3: High resolution TEM image for representative NiFe_2O_4 nanocrystals. (a) the specimen is tilted by 11° . NiFe_2O_4 nanocrystal is identified. The black lines guide the eyes to show the cubic symmetry of the secondary phase. (b) Another NiFe_2O_4 nanocrystals with the orientation of $(111)\parallel\text{ZnO}(0001)$ as confirmed by FFT patterns. The clearly visible planes are $\text{NiFe}_2\text{O}_4(111)$ with an angle of $\sim 71^\circ$ from the surface. In FFT patterns the dashed lines indicate the sets of lattice planes.

NiFe_2O_4 . However there are also some grains with [001] orientation, *e.g.* the one in Fig. 3(a). One also can see some moire fringes in the ZnO part due to the overlap of NiFe_2O_4 and ZnO.

Note that the NiFe_2O_4 grains (see Fig. 2) are as large as 20-40 nm, and larger than the values determined from XRD. However, one grain does not have to correspond to one NiFe_2O_4 nanocrystal. On the other hand, in the dark-field image all the grains show similar sizes as that in the bright field. This is due to the fact that these nanocrystals are well oriented. By high resolution TEM we examined more than 10 nanocrystals in different areas of the specimens. Their diameters are in the range of 10-20 nm, which is in a qualitative agreement with the XRD measurement.

B. Magnetic properties

By structural analysis, we have shown the formation of NiFe_2O_4 and CoFe_2O_4 nanocrystals inside the ZnO matrix. In this section, we will compare their magnetic properties. Fig. 4 shows the hysteresis loops measured at 5 K. The differences between NiFe_2O_4 and CoFe_2O_4 are significant. At 5 K, the coercivity of CoFe_2O_4 is 1900 Oe, and much larger than the coercivity of NiFe_2O_4 amounting to 280 Oe, *i.e.* one is a hard magnet, and the other is a soft one. For comparison the saturation magnetization of bulk crystals is also indicated in Fig. 4. NiFe_2O_4 nanocrystals have a slightly larger value than bulk NiFe_2O_4 , and a smaller value for CoFe_2O_4 nanocryst-

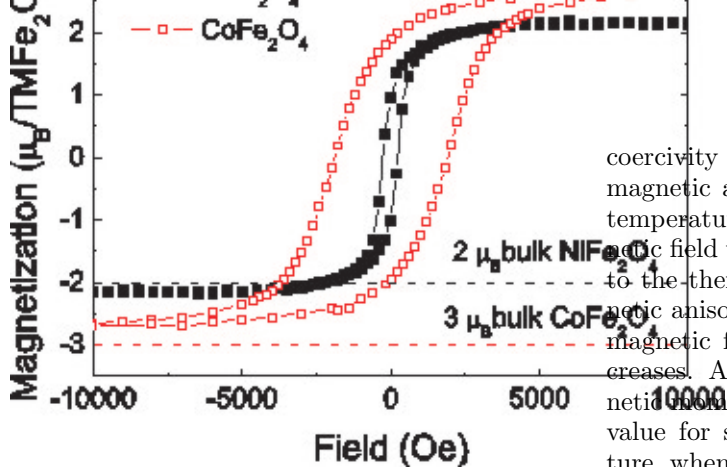


FIG. 4: Hysteresis loops measured at 5 K for NiFe_2O_4 and CoFe_2O_4 nanocrystals. They show drastic difference in coercivity field.

tals. This could be due to the cation site exchange between Ni^{2+} (Co^{2+}) and Fe^{3+} and will be discussed in section III C. However, another possibility is that there is a mixture of Ni^{2+} and Fe^{2+} at tetrahedral sites resulting in $(\text{Ni,Fe})\text{Fe}_2\text{O}_4$ ($\text{Ni}_{1-x}\text{Fe}_{2+x}\text{O}_4$). The magnetization for bulk Fe_3O_4 is $4.1 \mu_B$ per formula unit. To verify this, one needs to perform a precise local Fe, Ni(Co) concentration measurement. We performed an electron energy-loss spectroscopy (EELS) analysis to profile the composition of the ferrite nanocrystals during the TEM measurements. We could not probe an elementally resolvable EELS signal possibly due to the similar atomic number of the embedding ZnO matrix and the ferrite, given the complex element types (Fe, Co/Ni and Zn) within the probe area. Macroscopically, the appearance of Fe, Co, Ni is clearly revealed by x-ray absorption as shown later in Sec. III C. In literature the application of EELS in similar cases (embedded nanocrystals) is mainly for qualitative investigation^{22,23,24}. On the other hand, exposing the nanocrystals to the electron beam for a longer time results in a heavy beam damage and contamination of the specimens, as well as the structural modification of the nanocrystals²⁵.

Fig. 5 shows the temperature dependent saturation magnetization and coercivity. One sees clearly that the coercivity decreases exponentially with increasing temperature. This is expected for a magnetic nanoparticle system. According to the Stoner-Wohlfarth theory²⁶, the magnetic anisotropy energy E_A of a single domain particle can be expressed as:

$$E_A = KV \sin^2\theta, \quad (2)$$

where K is the magnetocrystalline anisotropy constant, V the volume of the nanoparticle, and θ is the angle between the magnetization direction and the easy axis of the nanoparticle. This anisotropy serves as the energy barrier to prevent the change of magnetization direction. When the size of magnetic nanoparticles is reduced to a critical value, E_A is comparable with thermal activation energy, $k_B T$, the magnetization direction of the nanoparticle can be easily moved away from the easy axis by thermal activation and/or an external magnetic field. The

coercivity of the nanoparticles is closely related to the magnetic anisotropy. At a temperature below blocking temperature T_B , the coercivity corresponds to a magnetic field which provides the required energy in addition to the thermal activation energy to overcome the magnetic anisotropy. As temperature increases, the required magnetic field (H_C) for overcoming the anisotropy decreases. At the temperature of 0 K, where all the magnetic moments are blocked, the coercivity is equal to the value for single domains. At a high enough temperature, when all moments fluctuate with a relaxation time shorter than the measuring time, coercivity equals zero. In the temperatures between the two extremes the coercivity H_C can be evaluated by the following formula²⁷:

$$H_C = H_{C0} \left[1 - \left(\frac{T}{T_B} \right)^{1/2} \right], \quad (3)$$

where H_{C0} is the coercivity at 0 K, and T_B the blocking temperature. Fig. 5(b) shows a plot of H_C as a function of $T^{1/2}$. For the NiFe_2O_4 system H_C roughly obeys a linear dependence on $T^{1/2}$ in the whole measured temperature range. The deduced blocking temperature lies around 360 K, which is rather close to the value found by the ZFC/FC magnetization as shown below. The poor fitting for the CoFe_2O_4 system may be due to the fact that the magnetocrystalline anisotropy energy of CoFe_2O_4 is much larger (two orders of magnitude) than NiFe_2O_4 . For a similar grain size the blocking temperature of CoFe_2O_4 can be much higher for NiFe_2O_4 . In such a case, the measured temperature range is not large enough compared to the high blocking temperature. This results in a large error in the fitting.

Fig. 6 shows the ZFC/FC magnetization curves measured at 50 Oe. An irreversible behavior is observed in ZFC/FC curves. Such an irreversibility originates from the anisotropy barrier blocking of the magnetization orientation in the nanoparticles cooled under zero field. The magnetization direction of the nanoparticles is frozen as the initial status at high temperature, *i.e.*, randomly oriented. At low temperature (5 K in our case), a small magnetic field of 50 Oe is applied. Some small nanoparticles with small magnetic anisotropy energy flip along the field direction, while the large ones do not. With increasing temperature, the thermal activation energy together with the field flips the larger particles. This process results in the increase of the magnetization in the ZFC curve with temperature. The size distribution of nanoparticles, *i.e.* the magnetic anisotropy is usually not uniform in the randomly arranged nanoparticle systems. The larger the particles, the higher the E_A , and a larger $k_B T$ is required to become superparamagnetic. The gradual increase and the small upturn at around 20 K in the ZFC curves is due to the size distribution of nanocrystals. In the ZFC curve for NiFe_2O_4 [Fig. 6(a)] a broad maximum is observed at around 330 K, while for CoFe_2O_4 [Fig. 6(a)] no maximum can be seen up to 350 K. The mean blocking temperature for CoFe_2O_4 is well above room temperature, which is evidenced also

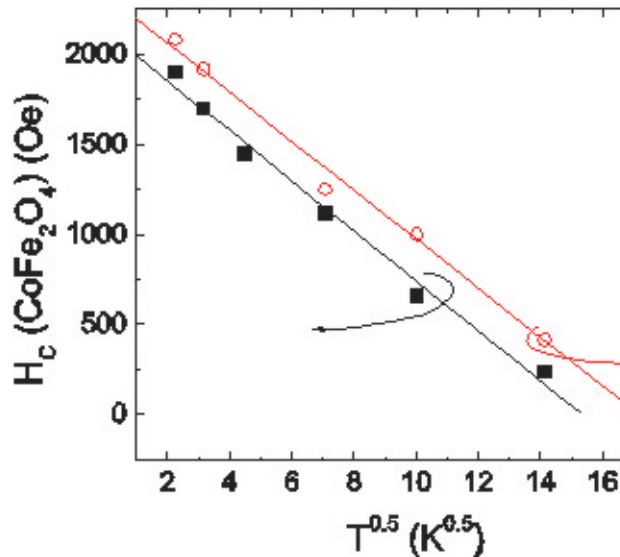
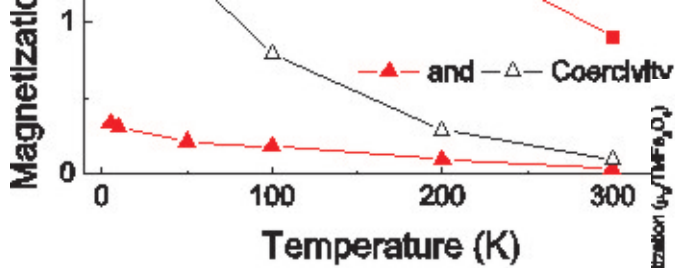


FIG. 5: (a) Temperature dependent saturation magnetization and coercivity for NiFe_2O_4 (red solid symbols) and CoFe_2O_4 (black open symbols). The solid lines are guides for eyes. (b) The plot of coercivity as a function of $T^{1/2}$.

from the rather large coercivity field of 80 Oe at 300 K (see Fig. 5). Note that the ZFC/FC magnetization of NiFe_2O_4 is much smaller than that of CoFe_2O_4 . This is due to the much larger coercivity field (magnetocrystalline constant K) of CoFe_2O_4 , which is well above the small applied field of 50 Oe.

Since the blocking temperature is closely related to the magnetic anisotropy energy E_A , one can evaluate the size of nanomagnets by the measured T_B . For a dc magnetization measurement in a small magnetic field by SQUID magnetometry, T_B is given by

$$T_{B,Squid} \approx \frac{KV}{30k_B}, \quad (4)$$

where K is the anisotropy energy density, V the particle volume, k_B the Boltzmann constant²⁸. K is 6.3×10^3 and $4.0 \times 10^5 \text{ Jm}^{-3}$ for bulk NiFe_2O_4 and CoFe_2O_4 , respectively, at room temperature^{29,30}. Due to its large magnetocrystalline anisotropy the maximum in ZFC curve of CoFe_2O_4 nanocrystals cannot be seen within the measured temperature range. That means the blocking temperature is much larger than 350 K, which corresponds to an average diameter of CoFe_2O_4 larger than 9 nm if assuming the value of K for a bulk CoFe_2O_4 . For NiFe_2O_4 nanocrystals, K is much smaller. Therefore, we can see a maximum at around 320 K in the ZFC magnetization curve. Using the K value for bulk NiFe_2O_4 , the average diameter of NiFe_2O_4 can be calculated and

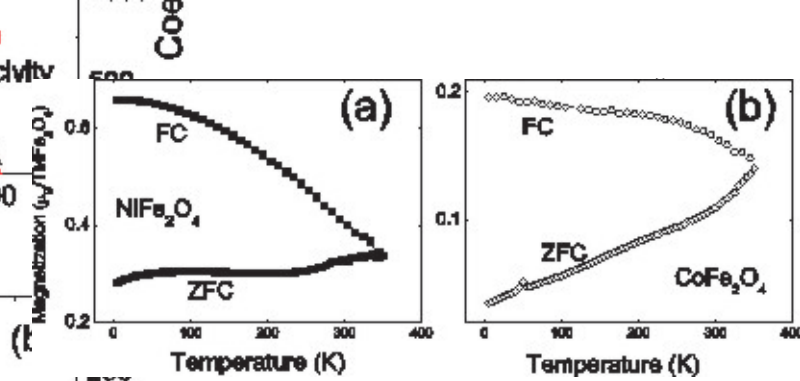


FIG. 6: ZFC/FC magnetization curves measured with a field of 50 Oe for (a) NiFe_2O_4 and (b) CoFe_2O_4 . Up to 350 K, no ZFC maximum was observed for CoFe_2O_4 .

amounts to 14 nm. This value, however, is larger than that deduced from XRD and TEM measurements. The large discrepancy is resulting from the underestimation of K by assuming the value of a bulk crystal. K can be largely enhanced due to strain, and surface effect in NiFe_2O_4 nanomagnets, but relatively less enhanced in CoFe_2O_4 ³¹. The later has been confirmed in strained epitaxial CoFe_2O_4 thin films³².

C. Electronic configuration

1. X-ray absorption spectra

The magnetic properties of 3d transition metal elements, such as Fe, Co and Ni are determined by the 3d valence electrons, which can be investigated by L-edge XAS measurements (transition from the 2p shell to the 3d shell). Fig. 7 shows the $L_{2,3}$ XAS of Fe, Co and Ni in the two samples, measured in TEY mode. The spectra of pure metals and some oxides are also shown for comparison. The metal spectra mainly show two broad peaks, reflecting the width of the empty d -bands, while the oxide spectra exhibit a considerable fine structure of the d -bands, the so-called multiplet structure. By comparison with corresponding XAS of pure metals, one can qualitatively conclude that metallic Fe, Co and Ni are not present in the samples. In Fig. 7(a) one can see the multiplet structure of Fe $L_{2,3}$ XAS. The most noticeable feature is the rather pronounced peak at the low energy part of the L_3 edge. This is a common feature for ferrite materials³³. Multiplet calculations for FeO and $\alpha\text{-Fe}_2\text{O}_3$ reveal that the shoulders at 705.5 eV and 718.5 eV [indicated by the vertical arrows in the Fig. 7(a)] are associated with Fe^{2+} ions³⁴. Note that these features disappear in the spectrum of Fe_2O_3 . Following these arguments, the Fe ions in our samples are mainly Fe^{3+} ions.

The Co- L_3 edge [Fig. 7(b)] is composed of a fine structure with four features, a small peak at 775.5 eV, the total maximum in absorption at 777 eV, followed by a shoulder at 778 eV and a further satellite at 780 eV. Since in this sample the Co is in pure Co^{2+} configuration, we can compare the spectrum with reference compounds namely CoO (spectrum taken from Ref. 35) and

$\text{Zn}_{0.75}\text{Co}_{0.25}\text{O}$ (spectrum taken from Ref. 36). Co^{2+} ions are at octahedral sites and at tetrahedral sites in CoO and $\text{Zn}_{0.75}\text{Co}_{0.25}\text{O}$, respectively. From the comparison of the overall shape and satellite structure our spectrum is more similar to that of CoO , and also similar to the XAS of CoFe_2O_4 presented in Ref. 37. We can conclude that the major part of Co^{2+} ions are at octahedral sites. In order to confirm this conclusion, we performed simulations of the local electronic structure around the Co^{2+} ions by means of full multiplet calculations using the TT-MULTIPLETS program^{38,39}. The energy levels of the initial ($2p^63d^7$) and final absorption state ($2p^53d^8$) are calculated by means of the corresponding Slater integrals which are subsequently reduced to 80% (corresponds to their atomic values). Then a tetrahedral or octahedral crystal field was considered using a crystal field parameter of $10 D_q = -1$ eV and $10 D_q = +1$ eV, respectively. Finally the calculated spectra were broadened with the experimental resolution for comparison. As displayed in Figure 8, one can see that the measured spectrum reasonably reproduces the features in the simulated octahedral coordination.

Fig. 7(c) shows the comparison of Ni $L_{2,3}$ with that in NiFe_2O_4 ⁴⁰. In the paper of Van der Laan *et al.*⁴⁰, the spectrum can be well simulated by considering Ni in an octahedral crystal-field coordination, *i.e.* Ni ions are fully at octahedral sites. However, the difference between the two spectra is quite clear, especially at the L_2 -edge. It could be due to the fact that Ni ions are partially located at tetrahedral sites.

The XAS spectra (Fig. 9) were also recorded at the O K-edge and Zn L-edge to prove the formation of ferrites and to check if Zn ions are significantly incorporated into ferrites. All shown spectra were measured in TEY mode, which is more sensitive to the near surface-region where the ferrite nanocrystals were formed. For the O K-edge, the difference between the NiFe_2O_4 , CoFe_2O_4 and ZnO is very clearly observed, which confirms the coordination change of O ions. Actually the spectra in Fig. 9(a) are very similar to those of Fe_2O_3 and Fe_3O_4 ⁴². Fig. 9(b) shows the comparison of the Zn L-edge spectra between ZnO embedded with NiFe_2O_4 , CoFe_2O_4 nanocrystals, and pure ZnO. The only difference is that the fine structure in the spectrum of ZnO is better resolved. This could be due to the lattice damage in ZnO by ion implantation. No significant amount of Zn has been incorporated into ferrites.

2. XMCD

Correspondingly, XAS recorded at 23 K in TEY (total electron yield) mode at the Fe, Co and Ni absorption edge revealed a pronounced dichroic behavior under magnetization reversal. XMCD is a difference spectrum of two XA spectra, one taken with left circularly polarized light, and the other with right circularly polarized light.

The XMCD signal at the Fe L_3 -edge XMCD for the

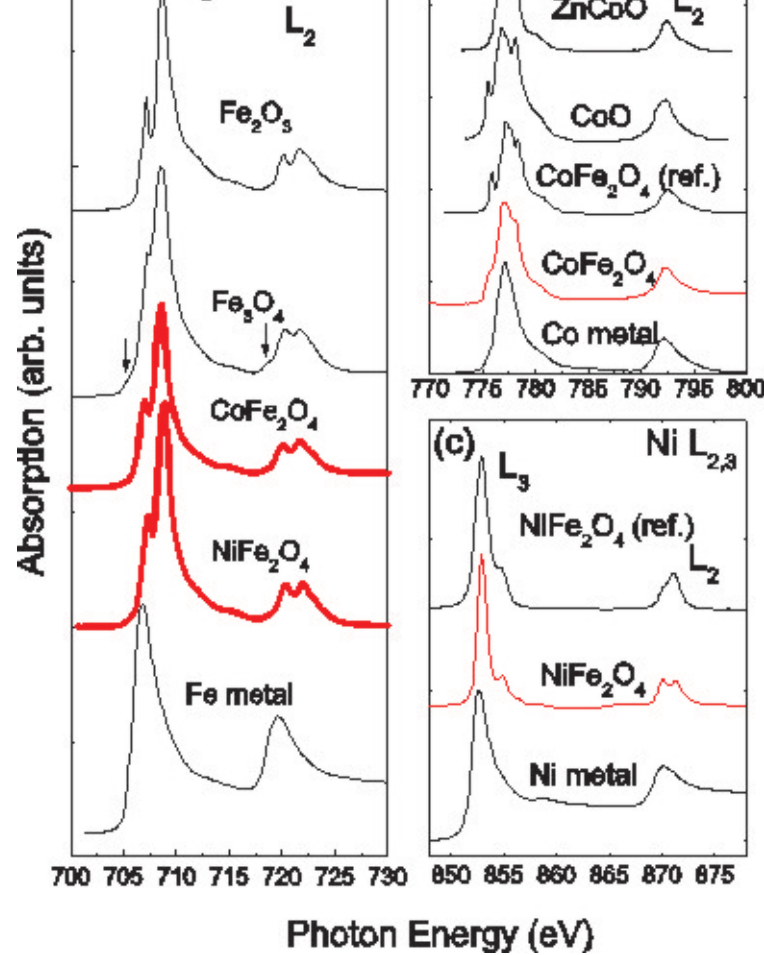


FIG. 7: XAS of NiFe_2O_4 and CoFe_2O_4 along with reference spectra from pure metal and oxides at the (a) Fe $L_{2,3}$ -edge, (b) Co $L_{2,3}$ -edge and (c) Ni $L_{2,3}$ -edge. The reference spectra are taken from published papers: Fe_2O_3 ⁴¹, Fe_3O_4 ⁴¹, CoO ³⁵, ZnCoO ³⁶, NiFe_2O_4 ⁴⁰ and CoFe_2O_4 ³⁷.

two samples is shown in Fig. 10(a) and (b). From the literature⁴³, peak A is attributed to Fe^{2+} at octahedral sites, while peaks B and C are due to Fe^{3+} at tetrahedral and octahedral sites, respectively. By comparing the relative height of peak A, B and C, we can draw some qualitative conclusions on the cation site distribution in NiFe_2O_4 and CoFe_2O_4 nanocrystals. Firstly, there are still some Fe^{2+} ions remaining, even if the ratio of implanted Ni(or Co) to Fe is exactly 1:2. This could be due to the fact that Ni(or Co) and Fe ions are not fully chemically reacted at the given annealing condition. Relatively, there are more Fe^{2+} ions at octahedral sites in CoFe_2O_4 than in NiFe_2O_4 . Secondly, part of Fe^{3+} ions are at tetrahedral sites in NiFe_2O_4 , while in CoFe_2O_4 the Fe^{3+} ions are mainly located at octahedral sites. Bulk NiFe_2O_4 and CoFe_2O_4 are inverse spinels. The Ni^{2+} and Co^{2+} ions are at octahedral sites, while half of the Fe^{3+} ions are at octahedral sites, and the other half are at tetrahedral sites. With this ordering, the moments of Fe ions at octahedral and tetrahedral sites cancel out, which results in a saturation magnetization of $2\mu_B$ per NiFe_2O_4 formula unit⁴⁴, and $3\mu_B$ per CoFe_2O_4 formula unit⁴⁵. However, in low dimensional spinels the cation distribution is often different from bulk materials^{44,46}.

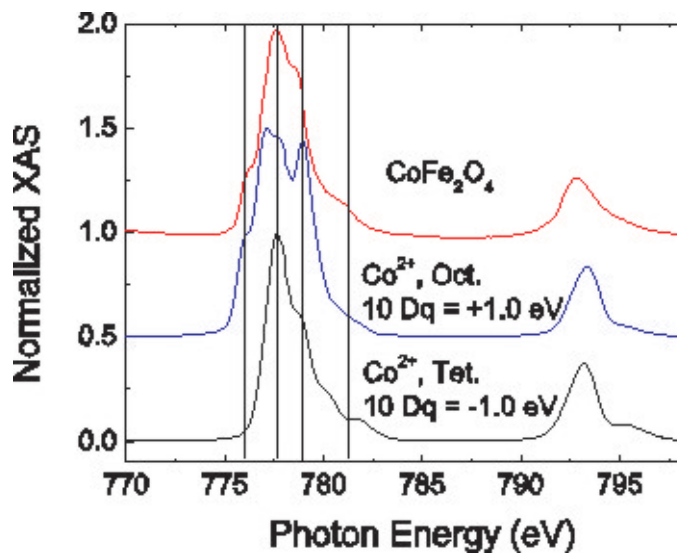


FIG. 8: The Co $L_{2,3}$ -edge XAS spectrum of CoFe_2O_4 along

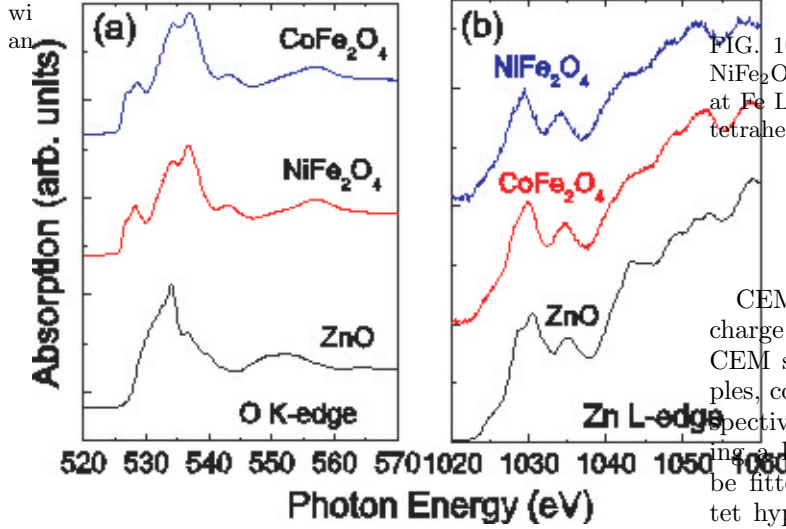


FIG. 9: The XA spectra of total electron yield (TEY) at the (a) O K-edge, and (b) Zn L-edge.

For the case of NiFe_2O_4 , if all Ni^{2+} replace the Fe^{3+} at tetrahedral sites, resulting in a normal spinel structure, the total magnetic moment can increase up to $4\mu_B$ per NiFe_2O_4 formula. Therefore, the larger magnetic moment in our NiFe_2O_4 nanocrystals as shown in Fig. 4 is probably due to a small amount of Ni^{2+} replacing the Fe^{3+} at tetrahedral sites. This cation distribution picture is in agreement with XAS analysis. However, as discussed in section III B, one needs a precise local concentration measurement to verify the ratio $Fe : Ni = 2 : 1$. Figs. 10(c) and (d) show the XMCD signal at the $L_{2,3}$ edge for Ni and Co, respectively. They are comparable with corresponding ferrites reported in literature^{33,40}. Note the fact that the relative strength of the XMCD signal of CoFe_2O_4 is much weaker than that of NiFe_2O_4 . This is due to their different coercivity fields. Due to the facility capability, a maximum field of 2000 Oe was applied during XAS measurements. The saturation field of CoFe_2O_4 is much larger than that of NiFe_2O_4 (see Fig. 4).

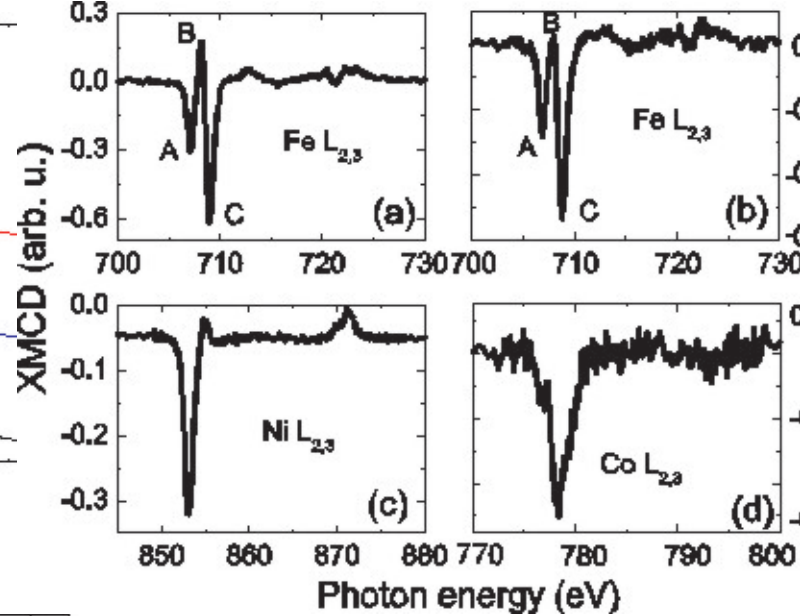


FIG. 10: XMCD at Fe, Ni and Co $L_{2,3}$ absorption edge. NiFe_2O_4 : (a) and (c). CoFe_2O_4 : (b) and (d). Peak labels at Fe L_{3} -edge: A for Fe^{2+} at octahedral sites, B for Fe^{3+} at tetrahedral sites and C for Fe^{3+} at octahedral sites⁴³.

3. CEMS

CEMS allows one to identify different site occupations, charge and magnetic states of ^{57}Fe . Fig. 11 shows the CEM spectra taken at room temperature for two samples, containing NiFe_2O_4 and CoFe_2O_4 nanocrystals, respectively. The two samples exhibit similar spectra. Using a least-squares computer program, the spectra can be fitted well by three components. Two sets of sextet hyperfine pattern and one doublet are resolved, all of which are related to Fe^{3+} . The hyperfine parameters calculated according to the evaluations of the spectra are given in Table I. The outer sextet (S1) with a larger magnetic hyperfine field corresponds to octahedral sites, while the inner one (S2) with a smaller magnetic hyperfine field to Fe^{3+} at tetrahedral sites^{47,48,49,50,51}. This feature of two sextets is a fingerprint that identifies ferrites. The relative line intensities of the sextets differ from those of a polycrystalline powder material indicating the presence of a texture. Note that the magnetic hyperfine field is considerably smaller than the values of around 50 T for typical NiFe_2O_4 or CoFe_2O_4 ^{47,51}, which results from the size effect⁵⁰. The doublet (D) is a more questionable component. Most probably it corresponds to smaller ferrite nanocrystals, which are superparamagnetic at room temperature. However, its isomer shift and electric quadrupole splitting values are considerably larger than the values reported in Ref. 51.

The cation distribution between the two sublattices generally determines the magnetic properties of the spinel system and can be calculated as a ratio between the relative areas of the respective hyperfine field distributions. As shown in Table I, there are more Fe^{3+} ions at octahedral sites for both samples. That means that the NiFe_2O_4 and CoFe_2O_4 nanocrystals are not purely

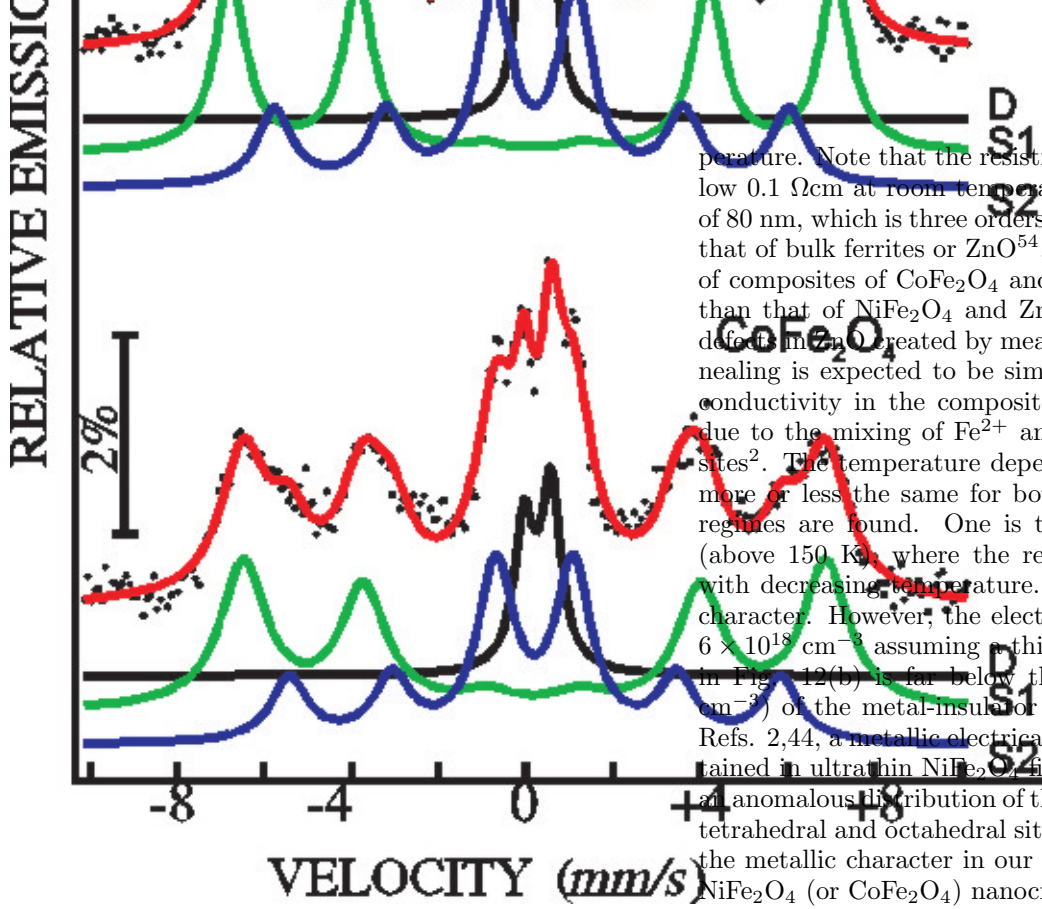


FIG. 11: Room temperature CEMS of NiFe₂O₄/ZnO and CoFe₂O₄/ZnO composites. The notations for the fitting lines are given as D (doublet) and S1, S2 (sextet).

inverted ferrites and Ni or Co ions partially occupy tetrahedral sites, which is in good agreement with the results of XAS.

D. Magneto-transport properties

Note that both bulk NiFe₂O₄ and CoFe₂O₄ are insulators with resistivity of 10²- 10³ Ωcm at room temperature^{2,9}. The resistivity of NiFe₂O₄ single crystals monotonically increases with decreasing temperature⁵². However, the corresponding thin film materials can be rather conductive². In ref. 2, the authors show that the NiFe₂O₄ films grown in pure Ar atmosphere have a room temperature resistivity three orders-of-magnitude smaller (ρ around 100 mΩcm). The temperature dependence $\rho(T)$ is similar to that of magnetite. On the other hand, ZnO single crystals grown by the hydrothermal method show a high bulk and surface resistivity, with the bulk conduction dominated by a deep donor⁵³. Typically, the free charge carrier concentration amounts to 1 × 10¹⁴ cm⁻³ and the mobility to 200 cm²V⁻¹s⁻¹ (Ref. 54). We measured the temperature dependence of the sheet resistance of the composites of NiFe₂O₄ and CoFe₂O₄ nanocrystals and ZnO from 20 or 40 to 290 K. Fig. 12(a) shows the Arrhenius plot, the sheet resistance R_s on a logarithmic scale as a function of reciprocal tem-

perature. Note that the resistivity of both samples is below 0.1 Ωcm at room temperature assuming a thickness of 80 nm, which is three orders of magnitude smaller than that of bulk ferrites or ZnO⁵⁴. The resistance/resistivity of composites of CoFe₂O₄ and ZnO is one order smaller than that of NiFe₂O₄ and ZnO. The amount of n-type defects in ZnO created by means of implantation and annealing is expected to be similar. Therefore, the larger conductivity in the composite of CoFe₂O₄ and ZnO is due to the mixing of Fe²⁺ and Fe³⁺ ions at octahedral sites². The temperature dependence of the resistance is more or less the same for both samples. Two different regimes are found. One is the high temperature part (above 150 K), where the resistance slightly decreases with decreasing temperature. This is a hint of metallic character. However, the electron concentration (around 6 × 10¹⁸ cm⁻³ assuming a thickness of 80 nm) as shown in Fig. 12(b) is far below the critical value (4 × 10¹⁹ cm⁻³) of the metal-insulator transition in n-ZnO⁵⁵. In Refs. 2,44, a metallic electrical conductivity has been obtained in ultrathin NiFe₂O₄ films, which is attributed to an anomalous distribution of the Fe and Ni cations among tetrahedral and octahedral sites. Therefore, we attribute the metallic character in our samples to the presence of NiFe₂O₄ (or CoFe₂O₄) nanocrystals. The second regime is in the temperature range below 150 K. In this regime, the samples show a semiconducting conductivity. The thermal activation energy E_a of free carriers can be determined according to the following equation:

$$\rho = e^{\frac{E_a}{k_B T}} + R_{s0}, \quad (5)$$

where k_B is the Boltzmann constant and R_{s0} a temperature independent contribution to the resistivity. In Fig. 12(a) the solid lines show the fitting, resulting in a thermal activation energy of ~28 meV for both samples. A similar thermal activation energy of 21 meV has been found in hydrothermally grown ZnO single crystals after high-temperature annealing⁵³. At low temperatures the impurities freeze out. In Ref. 52, the authors show that in their measured temperature range from around 77 K to room temperature the NiFe₂O₄ single crystals exhibit semiconducting conductivity, and the activation energy is around 60 meV. Fig. 12(b) displays the temperature dependent carrier concentration and Hall mobility. The sheet electron concentration increases with temperature and reaches to 4.8 × 10¹³ cm⁻². Its temperature dependence can be well fitted by the function $e^{-E_a/k_B T}$. Fig. 12(b) also shows the temperature-dependent mobility. The electron mobility μ reaches a maximum of above 900 cm²/Vs at 65 K. Actually such large electron mobility and concentration were also observed in ion implanted ZnO⁵⁶ and in virgin ZnO annealed in N₂⁵⁷.

We also measured the magnetic field dependent resistance (MR) for the composites of NiFe₂O₄ (CoFe₂O₄) nanocrystal and ZnO as shown in Fig. 13. MR is defined as

$$MR = (R[H] - R[0])/R[0]. \quad (6)$$

TABLE
and octa
splitting.

Sample
NiFe₂O₄
CoFe₂O₄

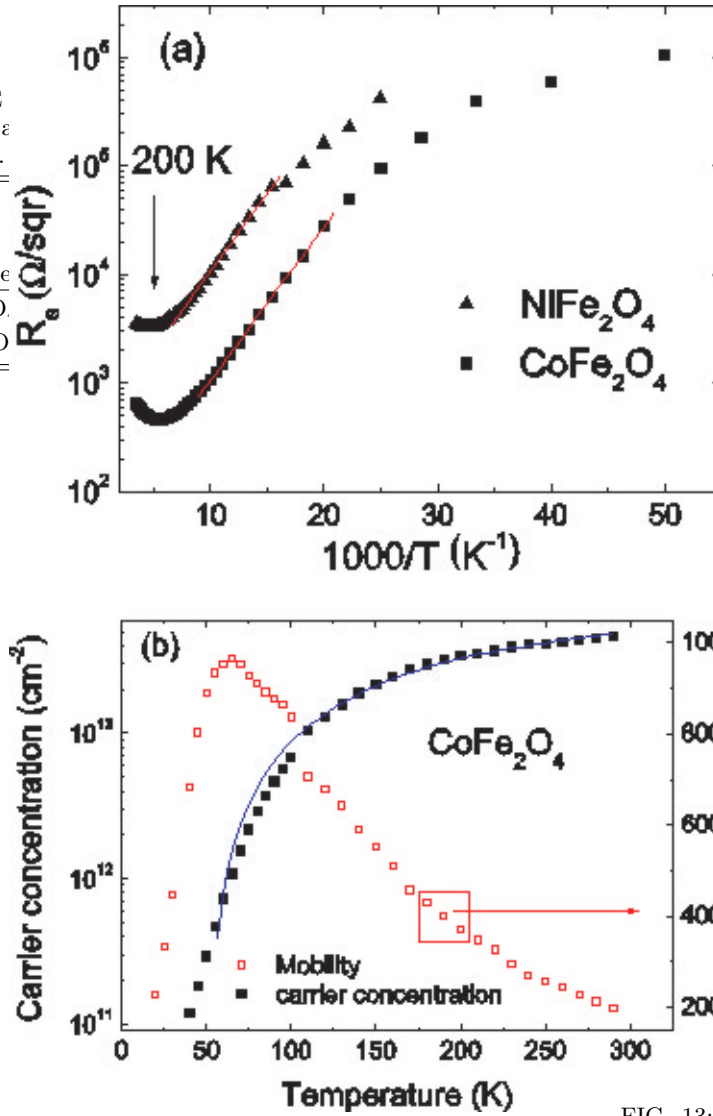


FIG. 12: (a) The temperature dependent sheet resistance (the solid lines show the linear fitting in the temperature range of 60-100 K), and (b) free carrier concentration and mobility of the composites of NiFe₂O₄ or CoFe₂O₄ nanocrystals and ZnO. The solid line is a fitting of carrier concentration by the function $e^{-E_a/k_B T}$.

The two samples exhibit a similar MR behavior. Only positive MR has been observed, and MR decreases quickly from around 16% (6 T) at 20 or 40 K to 0.2% (6 T) at 290 K. The overall shape of the field dependent MR is quadratic, and shows no sign of saturation. We attribute it to ordinary MR effect resulting from the curving of the electron trajectory due to Lorentz force in a magnetic field. The characteristic quantity is the Landau orbit, $L_H = (eH/\hbar c)^{-1/2}$, which is temperature independent. Another parameter is the dephasing length L_{Th} of electrons, the diffusing distance between two elastic scattering events, which decreases with increasing temperature. When the dephasing length is much smaller than the Landau orbit, $L_{Th}^2/L_H^2 \ll 1$, the magnetoresistance is quadratic and non saturating. Actually the field dependent MR can be fitted well as a H^2 dependence

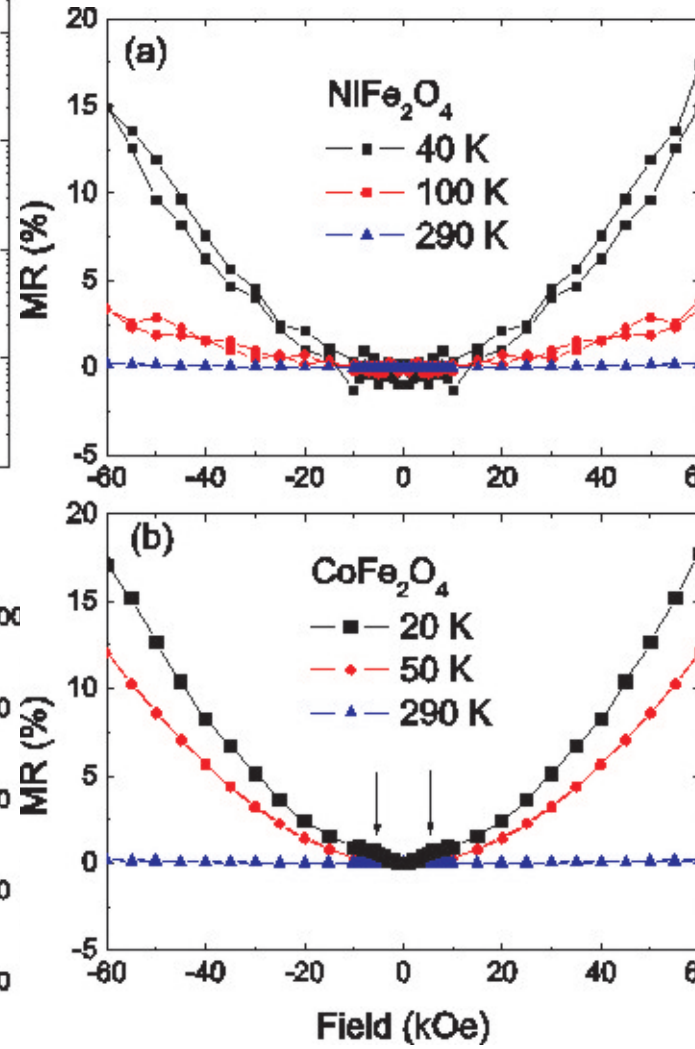


FIG. 13: The field dependent MR of (a) the composites of NiFe₂O₄ nanocrystals and ZnO and (b) the composites of CoFe₂O₄ nanocrystals and ZnO. The solid lines are guides to the eye.

(not shown). That means the dephasing length is very small in this sample due to the presence of NiFe₂O₄ or CoFe₂O₄ nanocrystals. In the literature a large positive MR up to several hundreds or thousands percent has been observed in regularly ordered nanowires⁵⁸ or nanocolumns⁵⁹. A non-saturating positive MR effect is expected to be useful for wide-range field sensing. A positive MR has also been observed in Co-doped ZnO films, and modelled by considering $s-d$ exchange^{55,60}. Note that the MR at 20 K in Fig. 13 exhibits a small contribution indicated by the arrows, which saturates at low fields. This contribution could be due to $s-d$ exchange considering that a small amount of Co²⁺ or Ni²⁺ ions remains in a diluted state. On the other hand, no negative MR has been observed, which often was found in the hybrid system of MnAs and GaAs^{61,62}.

The Hall resistivity

$$\rho_{xy} = R_H B + R_M \mu_0 M \quad (7)$$

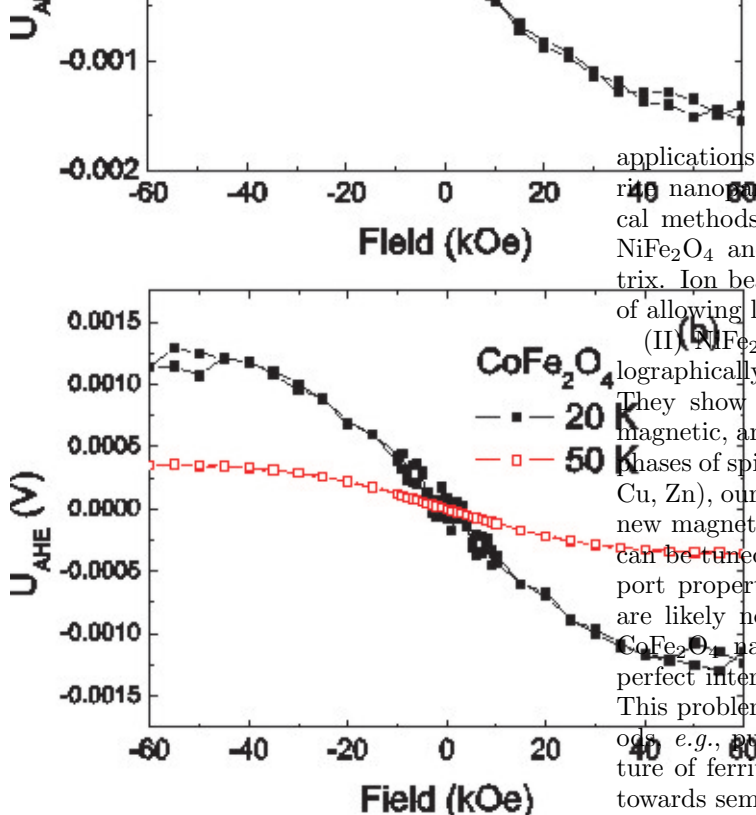


FIG. 14: Anomalous Hall voltage vs magnetic field for (a) the composites of NiFe₂O₄ nanocrystals and ZnO and (b) the composites of CoFe₂O₄ nanocrystals and ZnO.

is known to be a sum of the ordinary and anomalous Hall terms, where B is magnetic induction, μ_0 magnetic permeability, M magnetization, R_H the ordinary Hall coefficient, and R_M the anomalous Hall coefficient. The ordinary and anomalous Hall term is linear in B and M , respectively. After subtracting the linear part, the ordinary Hall effect, a clear AHE also has been observed in the two samples, as shown in Fig. 14. AHE vanishes at temperatures above 100 K. Obviously the AHE curve does not coincide with the magnetization curve as shown in Fig. 4 and Fig. 5. It is difficult to correlate the observed AHE to NiFe₂O₄ or CoFe₂O₄ nanocrystals. Usually, AHE is not expected or very weak for a semiconductor with embedded magnetic nanoparticles^{63,64}. If one considers that the shape of the AHE curves mimics the M-H curves, the AHE is likely due to some paramagnetic contributions or magnetism induced by intrinsic defects⁶⁵.

IV. CONCLUSIONS

(I) Nano-scaled ferrite materials attract considerable research attention due to their cation distribution and

applications as dielectric materials^{46,66,67,68}. Usually, ferrite nanoparticles are formed by mechanical or chemical methods. We have demonstrated the formation of NiFe₂O₄ and CoFe₂O₄ nanocrystals inside a ZnO matrix. Ion beam synthesis has its own obvious advantage of allowing lateral patterning⁶⁹.

(II) NiFe₂O₄ and CoFe₂O₄ nanoparticles are crystallographically oriented with respect to the ZnO matrix. They show similar structural properties, but different magnetic, and transport properties. Considering the rich phases of spinel ferrites (TMFe₂O₄, TM=Ni, Co, Fe, Mn, Cu, Zn), our results demonstrate the possibility to have a new magnet/semiconductor hybrid system. This system can be tuned over a large variety of magnetic and transport properties. However, the observed MR and AHE are likely not related to the presence of NiFe₂O₄ and CoFe₂O₄ nanocrystals. This could be due to the imperfect interface between nanocrystals and ZnO matrix. This problem could be solved by epitaxial growth methods, *e.g.*, pulsed laser deposition. A multilayered structure of ferrites/ZnO could be grown, and opens a path towards semiconducting spintronic devices.

(III) Our results suggest the possible integration of ferrites with semiconducting ZnO, which would allow the integration of microwave with semiconductor devices. The combination of ferrites and conventional semiconductors, *e.g.*, Si and GaAs, proves to be challenging due to the requirements of oxygen atmosphere and high temperature for ferrites¹¹.

V. ACKNOWLEDGEMENT

The authors (S.Z., Q.X. and H.S.) thank financial funding from the Bundesministerium für Bildung und Forschung (FKZ03N8708). Q. X. is supported by the National Natural Science Foundation of China (50802041). The Advanced Light Source is supported by the Director, Office of Science, Office of Basic Energy Sciences, of the U.S. Department of Energy under Contract No. DE-AC02-05CH11231.

During the press of this manuscript, we observed that an all-oxide ferromagnet/semiconductor (Fe₃O₄/ZnO) heterostructure has been realized by other groups using pulsed laser deposition⁷⁰.

* Electronic address: S.Zhou@fzd.de

¹ S. Chikazumi, *Physics of Ferromagnetism* (Oxford University Press, Oxford, 1997).

² U. Lüders, A. Barthélémy, M. Bibes, K. Bouzehouane, S. Fusil, E. Jacquet, J. P. Contour, J. F. Bobo, J. Fontcuberta, and A. Fert, *Adv. Mat.* **18**, 1733 (2006).

- ³ S. Zhou, K. Potzger, H. Reuther, G. Talut, F. Eichhorn, J. von Borany, W. Skorupa, M. Helm, and J. Fassbender, *J. Phys. D-Appl. Phys.* **40**, 964 (2007).
- ⁴ A. L. Geiler, A. Yang, X. Zuo, S. D. Yoon, Y. Chen, V. G. Harris, and C. Vittoria, *Phys. Rev. Lett.* **101**, 067201 (2008).
- ⁵ M. Ishikawa, H. Tanaka, and T. Kawai, *Appl. Phys. Lett.* **86**, 222504 (2005).
- ⁶ J. Takaobushi, H. Tanaka, T. Kawai, S. Ueda, J.-J. Kim, M. Kobata, E. Ikenaga, M. Yabashi, K. Kobayashi, Y. Nishino, D. Miwa, K. Tamasaku, T. Ishikawa, *Appl. Phys. Lett.* **89**, 242507 (2006).
- ⁷ U. Lüders, M. Bibes, K. Bouzehouane, E. Jacquet, J.-P. Contour, S. Fusil, J.-F. Bobo, J. Fontcuberta, A. Barthélémy, and A. Fert, *Appl. Phys. Lett.* **88**, 082505 (2006).
- ⁸ A. V. Ramos, M.-J. Guittet, J.-B. Moussy, R. Mattana, C. Deranlot, F. Petroff, and C. Gatel, *Appl. Phys. Lett.* **91**, 122107 (2007).
- ⁹ E. Snoeck, C. Gatel, R. Serra, G. BenAssayag, J.-B. Moussy, A. M. Bataille, M. Pannetier, and M. Gautier-Soyer, *Phys. Rev. B* **73**, 104434 (2006).
- ¹⁰ A. V. Ramos, T. S. Santos, G. X. Miao, M.-J. Guittet, J.-B. Moussy, and J. S. Moodera, *Phys. Rev. B* **78**, 180402 (2008).
- ¹¹ Z. Chen, A. Yang, A. Gieler, V. G. Harris, C. Vittoria, P. R. Ohodnicki, K. Y. Goh, M. E. McHenry, Z. Cai, T. L. Goodrich, K. S. Ziemer, *Appl. Phys. Lett.* **91**, 182505 (2007).
- ¹² Y. Suzuki, *Annu. Rev. Mater. Res.* **31**, 265 (2001).
- ¹³ J. Ziegler, J. Biersack, and U. Littmark, *The stopping and range of ions in matter* (Pergamon, New York, 1985).
- ¹⁴ S. Zhou, K. Potzger, J. von Borany, R. Grötzschel, W. Skorupa, M. Helm, and J. Fassbender, *Phys. Rev. B* **77**, 035209 (2008).
- ¹⁵ S. Zhou, K. Potzger, G. Talut, H. Reuther, J. von Borany, R. Grötzschel, W. Skorupa, M. Helm, J. Fassbender, N. Volbers, M. Lorenz, T. Herrmannsdörfer, *J. Appl. Phys.* **103**, 023902 (2008).
- ¹⁶ R. Brand, *Nucl. Instrum. Methods Phys. Res. B* **28**, 398 (1987).
- ¹⁷ A. Bonanni, A. Navarro-Quezada, T. Li, M. Wegscheider, Z. Matěj, V. Holý, R. T. Lechner, G. Bauer, M. Rovezzi, F. D'Acapito, M. Kiecana, M. Sawichi, T. Dietl, *Phys. Rev. Lett.* **101**, 135502 (2008).
- ¹⁸ B. D. Cullity, *Elements of X-ray Diffractions* (Reading, Addison-Wesley, 1978).
- ¹⁹ S. O. Kucheyev, J. S. Williams, C. Jagadish, J. Zou, C. Evans, A. J. Nelson, and A. V. Hamza, *Phys. Rev. B* **67**, 094115 (2003).
- ²⁰ S. Zhou, K. Potzger, D. Buerger, K. Kuepper, M. Helm, J. Fassbender, and H. Schmidt, *Nucl. Instr. and Meth. B* **267**, 1620 (2009).
- ²¹ S. Zhou, G. Talut, K. Potzger, A. Shalimov, J. Grenzer, W. Skorupa, M. Helm, J. Fassbender, E. Čížmár, S. A. Zvyagin, J. Wosnitza, *J. Appl. Phys.* **103**, 083907 (2008).
- ²² Y. J. Li, B. Zhang, W. Lu, Y. Wang, and J. Zou, *Appl. Phys. Lett.* **93**, 131919 (2008).
- ²³ Y. Wang, J. Zou, Y. Li, B. Zhang, and W. Lu, *Acta Mater.* **57**, 2291 (2009).
- ²⁴ M. Opel, K.-W. Nielsen, S. Bauer, S. T. Goennenwein, J. C. Cezar, D. Schmeisser, J. Simon, W. Mader, and R. Gross, *Eur. Phys. J. B* **63**, 437 (2008).
- ²⁵ B. Rellinghaus, S. Stappert, E. Wassermann, H. Sauer, and B. Spliethoff, *Eur. Phys. J. D* **16**, 249 (2001).
- ²⁶ E. C. Stoner and E. P. Wohlfarth, *IEEE Trans. Magn.* **27**, 3475 (1991).
- ²⁷ G. A. Candela and R. A. Haines, *Appl. Phys. Lett.* **34**, 868 (1979).
- ²⁸ M. Respaud, J. M. Broto, H. Rakoto, A. R. Fert, L. Thomas, B. Barbara, M. Verelst, E. Snoeck, P. Lecante, A. Mosset, J. Osuna, T. Ely, C. Amiens, B. Chaudret, *Phys. Rev. B* **57**, 2925 (1998).
- ²⁹ W. A. Yager, J. K. Galt, F. R. Merritt, and E. A. Wood, *Phys. Rev.* **80**, 744 (1950).
- ³⁰ R. M. Bozorth, E. F. Tilden, and A. J. Williams, *Phys. Rev.* **99**, 1788 (1955).
- ³¹ H. T. Jeng and G. Y. Guo, *J. Magn. Magn. Mater.* **240**, 436 (2002).
- ³² Y. Suzuki, R. B. van Dover, E. M. Gyorgy, J. M. Phillips, V. Korenivski, D. J. Werder, C. H. Chen, R. J. Cava, J. J. Krajewski, W. F. Peck, K. B. Do, *Appl. Phys. Lett.* **68**, 714 (1996).
- ³³ J. F. Hochepped, P. Saintavit, and M. Pileni, *J. Magn. Magn. Mater.* **231**, 315 (2001).
- ³⁴ J. P. Crocombette, M. Pollak, F. Jollet, N. Thromat, and M. Gautier-Soyer, *Phys. Rev. B* **52**, 3143 (1995).
- ³⁵ F. M. F. de Groot, M. Abbate, J. van Elp, G. A. Sawatzky, Y. J. Ma, C. T. Chen, and F. Sette, *J. Phys.-Condens. Matter* **5**, 2277 (1993).
- ³⁶ A. Barla, G. Schmerber, E. Beaupaire, A. Dinia, H. Bieber, S. Colis, F. Scheurer, J.-P. Kappler, P. Imperia, F. Nolting, F. Wilhelm, A. Rogalev, D. Müller, J. J. Grob, *Phys. Rev. B* **76**, 125201 (2007).
- ³⁷ G. van der Laan, E. Arenholz, R. V. Chopdekar, and Y. Suzuki, *Phys. Rev. B* **77**, 064407 (2008).
- ³⁸ F. M. F. de Groot, *J. Electron Spectrosc. Relat. Phenom.* **67**, 529 (1994).
- ³⁹ F. M. F. de Groot, *Coord. Chem. Rev.* **249**, 31 (2005).
- ⁴⁰ G. van der Laan, C. M. B. Henderson, R. A. D. Patrick, S. S. Dhesi, P. F. Schofield, E. Dudzik, and D. J. Vaughan, *Phys. Rev. B* **59**, 4314 (1999).
- ⁴¹ K. Kuepper, I. Balasz, H. Hesse, A. Winiarski, K. C. Prince, M. Matteucci, D. Wett, R. Szargan, E. Burzo, and M. Neumann, *Phys. Status Solidi A* **201**, 3252 (2004).
- ⁴² A. Gloter, A. Douiri, M. Tence, and C. Colliex, *Ultramicroscopy* **96**, 385 (2003).
- ⁴³ J. Takaobushi, M. Ishikawa, S. Ueda, E. Ikenaga, J.-J. Kim, M. Kobata, Y. Takeda, Y. Saitoh, M. Yabashi, Y. Nishino, D. Miwa, K. Tamasaku, T. Ishikawa, I. Satoh, H. Tanaka, K. Kobayashi, *Phys. Rev. B* **76**, 205108 (2007).
- ⁴⁴ U. Lüders, M. Bibes, J.-F. Bobo, M. Cantoni, R. Bertacco, and J. Fontcuberta, *Phys. Rev. B* **71**, 134419 (2005).
- ⁴⁵ V. N. Antonov, B. N. Harmon, and A. N. Yaresko, *Phys. Rev. B* **67**, 024417 (2003).
- ⁴⁶ C. N. Chinnasamy, A. Narayanasamy, N. Ponpandian, K. Chattopadhyay, H. Guerault, and J. M. Greneche, *J. Phys.-Condens. Matter* **12**, 7795 (2000).
- ⁴⁷ S. J. Kim, S. W. Lee, and C. S. Kim, *Jpn. J. Appl. Phys.* **40**, 4897 (2001).
- ⁴⁸ N. Ponpandian, A. Narayanasamy, C. N. Chinnasamy, N. Sivakumar, J.-M. Greneche, K. Chattopadhyay, K. Shinoda, B. Jeyadevan, and K. Tohji, *Appl. Phys. Lett.* **86**, 192510 (2005).
- ⁴⁹ J. P. Chen, C. M. Sorensen, K. J. Klabunde, G. C. Hadjipanayis, E. Devlin, and A. Kostikas, *Phys. Rev. B* **54**, 9288 (1996).
- ⁵⁰ S. Chakraverty, S. Mitra, K. Mandal, P. M. G. Nambissan,

- and S. Chattopadhyay, *Phys. Rev. B* **71**, 024115 (2005).
- ⁵¹ S. Mitra, K. Mandal, S. Sinha, P. M. G. Nambissan, and S. Kumar, *J. Phys. D-Appl. Phys.* **39**, 4228 (2006).
- ⁵² A. V. Zalesskii, M. K. Gubkin, T. M. Perekalina, and T. A. Khimich, *Crystallogr. Rep.* **45**, 678 (2000).
- ⁵³ G. H. Kassier, M. Hayes, F. D. Auret, M. Mamor, and K. Bouziane, *J. Appl. Phys.* **102**, 014903 (2007).
- ⁵⁴ K. Maeda, M. Sato, I. Niikura, and T. Fukuda, *Semicond. Sci. Technol.* **20**, S49 (2005).
- ⁵⁵ Q. Xu, L. Hartmann, H. Schmidt, H. Hochmuth, M. Lorenz, R. Schmidt-Grund, C. Sturm, D. Spemann, and M. Grundmann, *Phys. Rev. B* **73**, 205342 (2006).
- ⁵⁶ K. Potzger, K. Kuepper, Q. Xu, S. Zhou, H. Schmidt, M. Helm, and J. Fassbender, *J. Appl. Phys.* **104**, 023510 (2008).
- ⁵⁷ D. C. Look, B. Clafin, and H. E. Smith, *Appl. Phys. Lett.* **92**, 122108 (2008).
- ⁵⁸ K. Liu, C. L. Chien, P. C. Searson, and K. Yu-Zhang, *Appl. Phys. Lett.* **73**, 1436 (1998).
- ⁵⁹ M. Jamet, A. Barski, T. Devillers, V. Poydenot, R. Du-jardin, P. Bayle-Guillemaud, J. Rothman, E. Bellet-Amalric, A. Marty, J. Cibert, R. Mattana, S. Tatarenko, *Nat. Mater.* **5**, 653 (2006).
- ⁶⁰ Q. Xu, L. Hartmann, H. Schmidt, H. Hochmuth, M. Lorenz, D. Spemann, and M. Grundmann, *Phys. Rev. B* **76**, 134417 (2007).
- ⁶¹ P. J. Wellmann, J. M. Garcia, J. L. Feng, and P. M. Petroff, *Appl. Phys. Lett.* **73**, 3291 (1998).
- ⁶² H. Akinaga, J. De Boeck, G. Borghs, S. Miyanishi, A. Asamitsu, W. Van Roy, Y. Tomioka, and L. H. Kuo, *Appl. Phys. Lett.* **72**, 3368 (1998).
- ⁶³ S. R. Shinde, S. B. Ogale, J. S. Higgins, H. Zheng, A. J. Millis, V. N. Kulkarni, R. Ramesh, R. L. Greene, and T. Venkatesan, *Phys. Rev. Lett.* **92**, 166601 (2004).
- ⁶⁴ S. X. Zhang, W. Yu, S. B. Ogale, S. R. Shinde, D. C. Kundaliya, W.-K. Tse, S. Y. Young, J. S. Higgins, L. G. Salamanca-Riba, M. Herrera, L. F. Fu, N. D. Browning, R. L. Greene, T. Venkatesan, *Phys. Rev. B* **76**, 085323 (2007).
- ⁶⁵ Q. Xu, H. Schmidt, S. Zhou, K. Potzger, M. Helm, H. Hochmuth, M. Lorenz, A. Setzer, P. Esquinazi, C. Me-neckke, M. Grundmann, *Appl. Phys. Lett.* **92**, 082508 (2008).
- ⁶⁶ S. A. Oliver, H. H. Hamdeh, and J. C. Ho, *Phys. Rev. B* **60**, 3400 (1999).
- ⁶⁷ M. Bohra, S. Prasad, N. Kumar, D. S. Misra, S. C. Sahoo, N. Venkataramani, and R. Krishnan, *Appl. Phys. Lett.* **88**, 262506 (2006).
- ⁶⁸ S. Thakur, S. C. Katyal, and M. Singh, *Appl. Phys. Lett.* **91**, 262501 (2007).
- ⁶⁹ J. Fassbender and J. McCord, *J. Magn. Magn. Mater.* **320**, 579 (2008).
- ⁷⁰ A. Nielsen, A. Brandlmaier, M. Althammer, W. Kaiser, M. Opel, J. Simon, W. Mader, S. T. B. Goennenwein, and R. Gross, *Appl. Phys. Lett.* **93**, 162510 (2008).